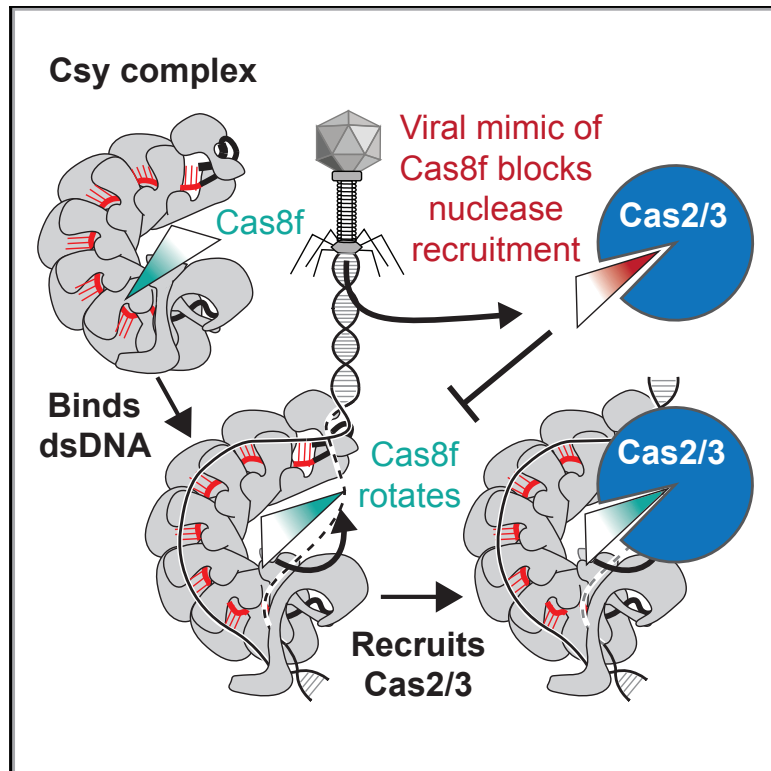


Molecular Cell

Structure Reveals a Mechanism of CRISPR-RNA-Guided Nuclease Recruitment and Anti-CRISPR Viral Mimicry

Graphical Abstract



Authors

MaryClare F. Rollins,
Saikat Chowdhury, Joshua Carter, ...,
C. Martin Lawrence, Gabriel C. Lander,
Blake Wiedenheft

Correspondence

glander@scripps.edu (G.C.L.),
bwiedenheft@gmail.com (B.W.)

In Brief

The structure of a CRISPR-RNA-guided surveillance complex bound to dsDNA reveals a viral immune suppressor protein (AcrIF3) that mimics a critical subunit of the surveillance complex, which helps explain the mechanism of nuclease recruitment for degradation of foreign DNA.

Highlights

- Structure of the type I-F CRISPR-RNA-guided surveillance complex bound to dsDNA
- R-loop formation drives a conformational change that signals nuclease recruitment
- Viral anti-CRISPR is a mimic of the C-terminal helical bundle of Cas8f



Structure Reveals a Mechanism of CRISPR-RNA-Guided Nuclease Recruitment and Anti-CRISPR Viral Mimicry

MaryClare F. Rollins,^{1,4} Saikat Chowdhury,^{3,4,5} Joshua Carter,^{1,6} Sarah M. Golden,¹ Heini M. Miettinen,¹ Andrew Santiago-Frangos,¹ Dominick Faith,¹ C. Martin Lawrence,² Gabriel C. Lander,^{3,7,*} and Blake Wiedenheft^{1,7,8,*}

¹Department of Microbiology and Immunology, Montana State University, Bozeman, MT 59717, USA

²Department of Chemistry and Biochemistry, Montana State University, Bozeman, MT 59717, USA

³Department of Integrative Structural and Computational Biology, Scripps Research Institute, La Jolla, CA, USA

⁴These authors contributed equally

⁵Present address: Department of Biochemistry and Cell Biology, Stony Brook University, Stony Brook, NY 11794, USA

⁶Present address: Nuffield Department of Medicine, University of Oxford, John Radcliffe Hospital, Headley Way, Oxford OX3 9DU, UK

⁷Senior author

⁸Lead Contact

*Correspondence: glander@scripps.edu (G.C.L.), bwiedenheft@gmail.com (B.W.)

<https://doi.org/10.1016/j.molcel.2019.02.001>

SUMMARY

Bacteria and archaea have evolved sophisticated adaptive immune systems that rely on CRISPR RNA (crRNA)-guided detection and nuclease-mediated elimination of invading nucleic acids. Here, we present the cryo-electron microscopy (cryo-EM) structure of the type I-F crRNA-guided surveillance complex (Csy complex) from *Pseudomonas aeruginosa* bound to a double-stranded DNA target. Comparison of this structure to previously determined structures of this complex reveals a ~180-degree rotation of the C-terminal helical bundle on the “large” Cas8f subunit. We show that the double-stranded DNA (dsDNA)-induced conformational change in Cas8f exposes a Cas2/3 “nuclease recruitment helix” that is structurally homologous to a virally encoded anti-CRISPR protein (AcrIF3). Structural homology between Cas8f and AcrIF3 suggests that AcrIF3 is a mimic of the Cas8f nuclease recruitment helix.

INTRODUCTION

CRISPR and their associated genes (*cas*) are essential components of sophisticated adaptive immune systems that are widespread in bacteria and archaea but are not found in eukaryotic genomes or eukaryotic organelles that originated from bacteria (e.g., mitochondria and chloroplasts) (Hille et al., 2018; Koonin et al., 2017; Marraffini, 2015; Mohanraju et al., 2016; van Houte et al., 2016). Microbial CRISPR-Cas systems are divided into class 1 systems, which rely on multi-subunit CRISPR RNA (crRNA)-guided surveillance complexes, and class 2 systems, which rely on a single multi-domain protein that serves as a crRNA-guided effector nuclease (Koonin et al., 2017; Makarova et al., 2015). The simple composition and programmable versatility of the class 2 nucleases (i.e., Cas9, Cas12, and Cas13) has

attracted considerable attention for diverse applications in genome engineering (Murugan et al., 2017; Shmakov et al., 2017; Wilkinson and Wiedenheft, 2014). However, these systems are relatively rare in nature, occurring in fewer than 10% of sequenced bacterial and archaeal genomes, while the class 1 systems represent the remaining 90% of adaptive immune systems observed in nature (Makarova et al., 2015).

Class 1 systems are divided into three different types (I, III, and IV) that are further divided into subtypes based on gene sequences and organization of the operon. The type I systems are the most abundant, widespread, and diverse of these systems, which include seven distinct subtypes (i.e., I-A through I-F; I-U) (Koonin et al., 2017; Makarova et al., 2015). Despite this diversity, all type I systems rely on multi-subunit crRNA-guided surveillance systems to identify foreign DNA (Jackson and Wiedenheft, 2015), which is subsequently eliminated by the *trans*-acting nuclease-helicase Cas3 (Brouns et al., 2008; Gong et al., 2014; Huo et al., 2014; Jackson et al., 2014; Loeff et al., 2018; Mulepati and Bailey, 2013; Sinkunas et al., 2011; Westra et al., 2012). In most type I systems, Cas2 and Cas3 are separate proteins involved in adaptation (i.e., integration of foreign DNA into the CRISPR) and interference (i.e., crRNA-guided target degradation), respectively (Makarova et al., 2015). However, in I-F systems, these proteins are fused into a single polypeptide (i.e., Cas2/3), which forms a homodimer that assembles with four molecules of the Cas1 adaptation protein (Fagerlund et al., 2017; Richter et al., 2012; Rollins et al., 2017). Within the Cas1-2/3 complex, the Cas1 proteins repress Cas2/3 endonuclease activity, which must be activated by the target bound type I-F surveillance complex (Csy complex) (Rollins et al., 2017). While previously determined structures of the Cas1-2/3 complex and the Csy surveillance complex provide mechanistic insights into their respective functions, the molecular mechanisms that govern Cas2/3 recruitment and nuclease activation remain obscure.

To understand the mechanism of target DNA recognition by the Csy surveillance complex, Guo et al. (2017) recently determined the structures of the Csy complex before DNA binding and after binding to a partially duplexed DNA target. These



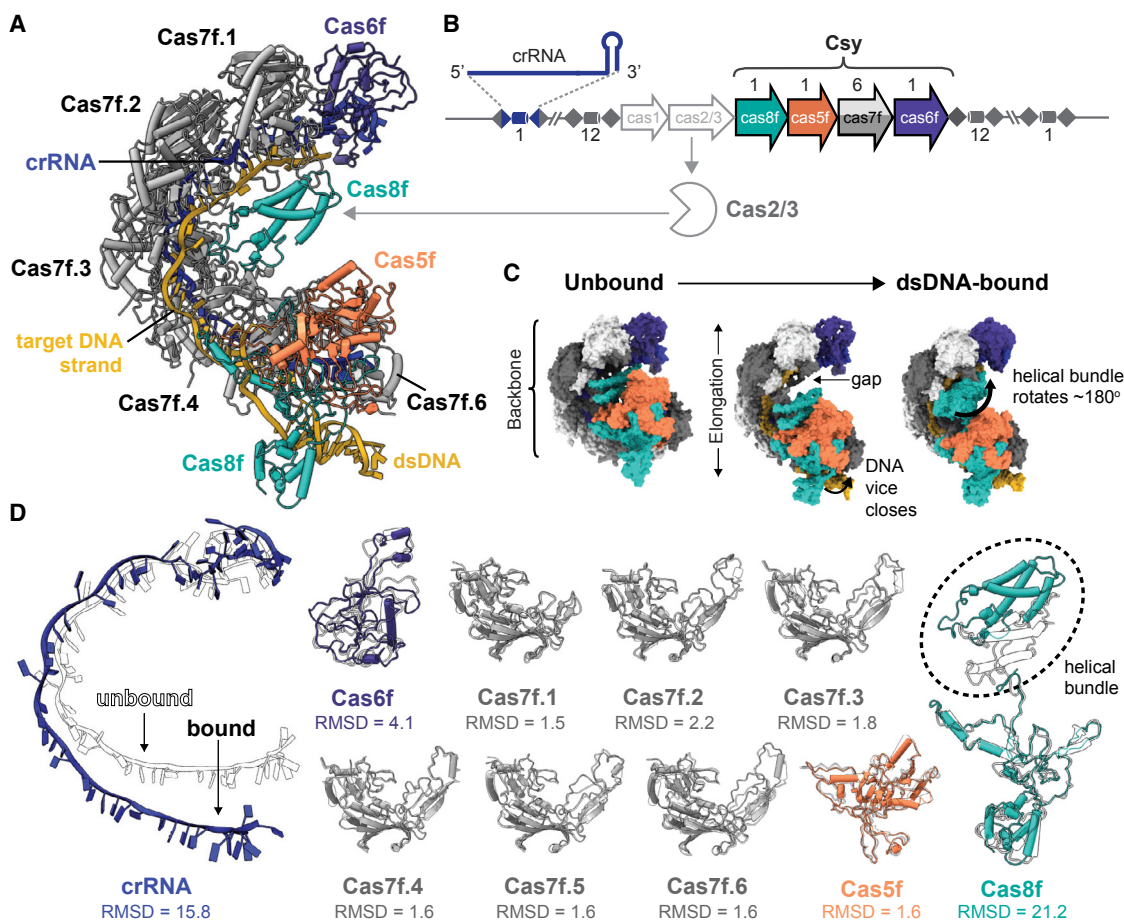


Figure 1. DNA Binding Induces Conformational Changes in the Csy Complex

(A) Atomic model of the type I-F crRNA-guided surveillance complex (Csy complex) from *P. aeruginosa* (PA14) bound to a dsDNA target.

(B) The type I-F CRISPR-Cas immune system in *P. aeruginosa* (PA14) consists of six *cas* genes flanked by two CRISPR loci. Colored arrows indicate subunits within the Csy complex. The binding site for Cas2/3 (pac-man) is indicated with a gray arrow.

(C) Schematic representation of the conformational change in the Csy complex, from unbound to dsDNA bound. From left to right: the unbound complex (PDB: 6B45), Csy bound to a partially duplexed dsDNA (PDB: 6B44), and the dsDNA-bound complex (PDB: 6NE0).

(D) Individual subunits of the Csy complex shown in their unbound (outlines) and target-bound (colored) conformations. The RMSD for equivalently positioned C-alpha atoms is indicated beneath each subunit.

structures explain the mechanism of protospacer adjacent motif (PAM) recognition and reveal an elongation of the complex that is driven by crRNA-guided hybridization to cDNA. However, the mechanism by which the nuclease is recruited to the target-bound complex was not elucidated.

Here, we use cryo-electron microscopy (cryo-EM) to determine the ~ 3.2 -Å-resolution structure of the Csy complex from *Pseudomonas aeruginosa* bound to an 80-bp double-stranded DNA (dsDNA) target (Figure 1). The structure reveals dramatic conformational changes that are not observed in the previously determined structures. In combination with biochemical methods, we show that these structural differences have significant functional consequences. Specifically, this work explains how R-loop formation created by crRNA-guided strand invasion of a dsDNA target is necessary for driving a ~ 180 -degree rotation of the C-terminal helical bundle on the “large” Cas8f subunit. This conformational change presents a “nuclease recruitment helix”

that is buried in the unbound structure. Additionally, we show that the helical bundle of Cas8f is structurally homologous to a virally encoded anti-CRISPR protein (AcrIF3) that suppresses immune function by mimicking the nuclease recruitment helix on Cas8f, raising the possibility that *cas* genes may sometimes serve as genetic fodder for the evolution of anti-CRISPR.

RESULTS

DNA Binding Induces Conformational Changes in the Csy Complex

To determine the mechanism of foreign DNA recognition and Cas2/3 recruitment by the Csy complex, we determined the ~ 3.2 Å cryo-EM structure of the Csy complex from *P. aeruginosa* (strain PA14) bound to an 80-bp dsDNA target containing a protospacer and a PAM (Figures 1A and S1–S3; Tables S1 and S2). The cryo-EM reconstruction was of sufficient

quality for atomic modeling (see [STAR Methods](#)). A 15-residue linker within the Cas8f subunit could not be modeled due to lack of density in the reconstructed map, likely due to intrinsic flexibility. Although the density for the 3' end of the R-loop was observed, this region was not sufficiently ordered to accurately model the nucleobases, and thus only the sugar-phosphate backbone was built into the model ([Figure S3E](#)).

The Csy complex is a multi-subunit crRNA-guided surveillance complex composed of an unequal stoichiometry of four different CRISPR-associated (Cas) proteins and a single 60-nt crRNA (Cas8f₁:Cas5f₁:Cas7f₆:Cas6f₁:crRNA₁) ([Chowdhury et al., 2017](#); [Guo et al., 2017](#); [Peng et al., 2017](#); [Wiedenheft et al., 2011](#); [Figure 1B](#)). The complex assembles into an asymmetric spiral that is capped at one end by Cas6f (i.e., the “head”) and on the other by a heterodimer of Cas5f and Cas8f, which form the “tail.” Cas6f (formerly Csy4) is a CRISPR RNA processing enzyme that binds to and cleaves CRISPR RNA stem-loop structures consisting of palindromic repeat sequences ([Haurwitz et al., 2010](#); [Przybilski et al., 2011](#); [Sternberg et al., 2012](#)). After cleavage, Cas6f remains stably associated with the 3' end of the crRNA, and six Cas7f subunits oligomerize along the crRNA, forming the “backbone” of the complex ([Chowdhury et al., 2017](#); [Guo et al., 2017](#); [Peng et al., 2017](#); [Figure 1A](#)). In the tail, the 5' end of the crRNA is anchored by a network of interactions within the stable heterodimer formed by Cas5f and the N-terminal domain of Cas8f.

The dsDNA target-bound structure undergoes significant conformational rearrangements relative to both the unbound complex and the complex bound to a partial duplex ([Guo et al., 2017](#); [Figure 1C](#); [Video S1](#)), while retaining the same overall morphology (head, backbone, and tail). The transition to the dsDNA-bound conformation can be broadly described in three coordinated movements. First, a positively charged “DNA vise” formed by the N-terminal segment of Cas8f and the opposing face of Cas7f.6 closes around the dsDNA. In this position, two loops of Cas8f insert into the DNA minor groove, where specific residues interact with the PAM. Cas8f and Cas5f form a stable heterodimer ([Chowdhury et al., 2017](#); [Wiedenheft et al., 2011](#)), and movement of the N terminus of Cas8f coincides with a ~25Å rigid-body translation of Cas5f away from the head of the complex. This action, combined with hybridization between the target DNA and the complementary crRNA spacer, results in an elongation of the Cas7f backbone. Compared to the unbound conformation, the length of the backbone as measured from Cas7f.1 to Cas7f.6 is extended ~18 Å in the target-bound structure, which opens the tight helical spiral, exposing an average of ~145 Å² of formerly buried surface area between adjacent Cas7 subunits. The elongated conformation also creates a gap between the head and the tail of the complex that is necessary for a ~180° rotation of the helical bundle of Cas8f ([Figure 1C](#)).

Transition to the dsDNA-bound conformation is primarily accomplished by rigid-body rearrangements of the Cas subunits; structures of individual subunits reveal few changes relative to their unbound state ([Figure 1D](#)). Notably, the first two conformational changes (i.e., closing of the DNA vise and elongated Cas7f backbone) are evident in a recent cryo-EM structure of the Csy complex bound to a partial dsDNA target

([Guo et al., 2017](#)). However, rotation of the Cas8f helical bundle is absent in this structure, suggesting that this rearrangement is dependent on R-loop formation. The dsDNA-bound structure presented here also reveals a “locked” conformation not observed in previous models, where regions of Cas7f.2 and Cas7f.3 fold over the DNA target strand and contact the helical bundle of Cas8f, completely encasing the cDNA. Thus, target binding triggers dramatic conformational changes in the Csy complex, and some of these rearrangements are only observed when Csy binds a fully duplexed DNA target.

Cas8f Mediates dsDNA Binding and PAM Recognition

In type I systems, crRNA-guided surveillance complex initially engages DNA through non-sequence-specific electrostatic interactions with dsDNA, followed by sequence-specific interactions with the PAM ([Jung et al., 2017](#); [Redding et al., 2015](#); [Rollins et al., 2015](#); [Xue et al., 2017](#)). PAMs are short sequence motifs that flank the protospacer in foreign targets only, thereby distinguishing self-DNA from non-self-DNA ([Leenay et al., 2016](#); [Mojica et al., 2009](#); [Figure 2A](#)). PAM recognition by the surveillance complex destabilizes the DNA duplex and facilitates crRNA-guided strand invasion ([Guo et al., 2017](#); [Hayes et al., 2016](#); [Xiao et al., 2017](#)). Hybridization of the crRNA guide to the cDNA displaces the non-complementary strand, resulting in an R-loop structure ([Blosser et al., 2015](#); [Hayes et al., 2016](#); [Hochstrasser et al., 2016](#); [Pausch et al., 2017](#); [Rutkauskas et al., 2015](#); [Szczelkun et al., 2014](#); [van Erp et al., 2018](#); [Xiao et al., 2017](#)). The N-terminal domain of Cas8f and the opposing face of the terminal Cas7f subunit (Cas7f.6) form a positively charged vise that closes around dsDNA ([Figures 2B and 2C](#); [Chowdhury et al., 2017](#); [Guo et al., 2017](#)). DNA binding results in a conformational change that moves the positively charged arm of Cas8f (R24–R58) ~15 Å into the closed position, clamping the complex onto the dsDNA ([Figure 2C](#)). In addition, closing of the DNA vise positions two loops of Cas8f in the DNA minor groove, which coincides with local distortion of the helix and separation of the DNA strands ([Figures 2D–2F](#); [Videos S1 and S2](#)). Asparagine 111 (N111) and asparagine 250 (N250) of Cas8f are positioned within hydrogen bonding distance of the –2 and –1 positions of the PAM, respectively ([Figure 2D](#)). To verify the role of these residues in PAM recognition, we introduced alanine mutations at N111 and N250. While we were unable to purify the Csy complex containing the N111A mutation in Cas8f, the N250A mutant expressed and purified like wild-type (WT) complex ([Figure S4](#)). We performed electrophoretic mobility shift assays (EMSAs) with both WT and Cas8f N250A Csy complex ([Figures 2G and S4](#)). Compared to WT, the Cas8f N250A mutation decreased DNA binding affinities by >3 orders of magnitude.

The DNA strands separate at the first base pair of the protospacer (i.e., position +1). Strand splitting is facilitated by lysine 247 (K247), which forms a wedge that inserts between the strands above the PAM ([Figures 2D–2F](#)). To test the requirement of this wedge for target binding, we introduced a charge-swap mutation (K247E) in Cas8f and measured its impact using EMSAs. The K247E mutation results in a binding defect and corroborates previous structural observations of the Csy complex bound to a partially duplexed DNA target ([Figure 2G](#);

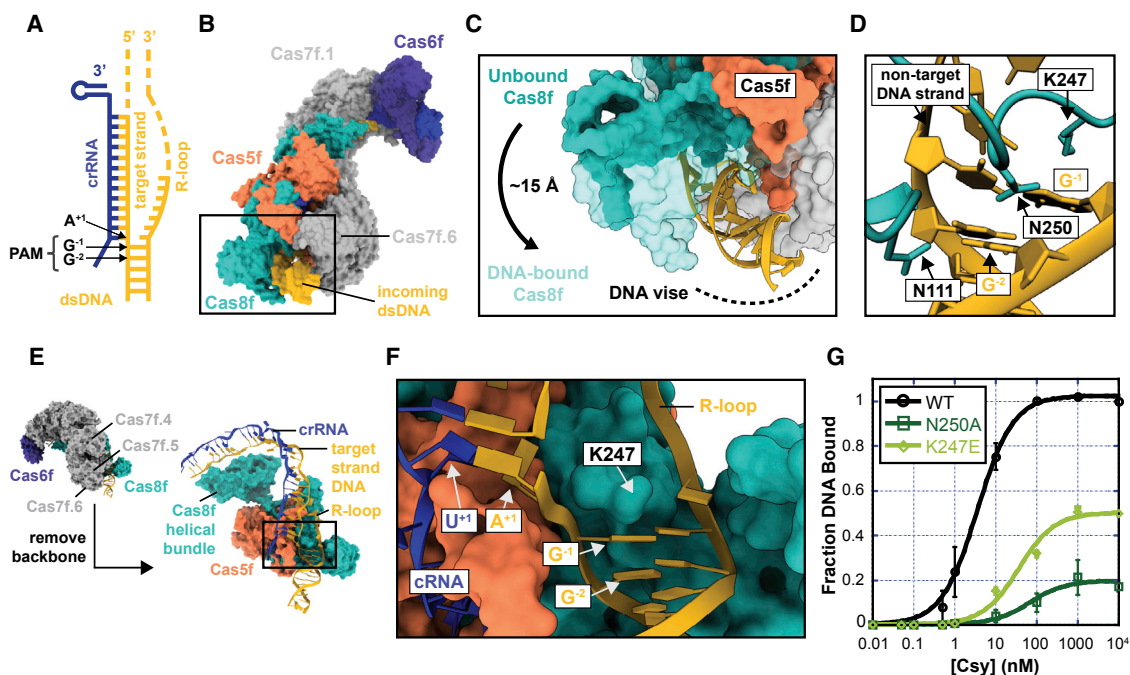


Figure 2. Cas8f and Cas7.6 Form a Vise that Closes on dsDNA and Recognizes the PAM

(A) Schematic of 80-nt dsDNA target bound by the Csy complex. Dashed segments of the DNA (yellow) represent regions of the target that were not sufficiently ordered and could not be reliably modeled.

(B) Surface representation of the dsDNA-bound Csy complex. The DNA vise (black box) is formed by the N-terminal domain of Cas8f and the opposing face of Cas7.6f.

(C) Conformational change of the vise upon dsDNA binding. The positively charged arm of Cas8f (R24–R58) moves ~15 Å into the closed position.

(D) Two loops of Cas8f are inserted into the minor groove. Asparagine 111 (N111) is positioned within hydrogen bonding distance of the second base pair of the PAM (i.e., G-C⁻²), and asparagine 250 (N250) is oriented toward the -1 G of the PAM (G⁻¹).

(E) Sidelong view of the dsDNA-bound Csy complex. The box highlights Cas8f-mediated DNA strand splitting.

(F) Lysine 247 (K247) acts as a wedge, separating the strands and positioning the first nucleotide of the target sequence for base-pairing with the first nucleotide of the crRNA guide.

(G) Electrophoretic mobility shift assays performed with radiolabeled dsDNA substrates show that Cas8f mutations N250A or K247A result in reduced crRNA-guided DNA binding. Error bars represent SD; n = 3.

Guo et al., 2017). In fact, comparison of the two structures suggests the mechanism of PAM recognition is unchanged by the presence or absence of an R-loop. The root-mean-square deviation (RMSD) for equivalently positioned C-alpha atoms in the Cas8f NTDs is 1.69 Å. This is consistent with an early role for PAM recognition in target binding, prior to formation and coordination of the R-loop.

The Interface between Cas8f and Cas5f Forms an R-Loop Binding Channel

PAM recognition induces local distortion of the DNA duplex that facilitates crRNA-guided hybridization to the cDNA target, which displaces the non-cDNA strand (R-loop). Although the R-loop itself is not resolved to high resolution, the cryo-EM density is consistent with a span of nine nucleosides that are positioned along a positively charged channel formed by residues in Cas8f (K28, K31, K119, R207, R219, R258, and R259) and Cas5f (K76 and R77) (Figures 3A and S3; Video S2). While the density for the remaining nucleosides of the flexible R-loop are insufficiently resolved for atomic modeling, the positively charged channel continues along Cas5f and the helical bundle

of Cas8f, terminating between arginine-rich helices on Cas5f (K171, R175, R178, and R179) and Cas8f (R293, R299, R302, and R306) (Figure 3B). We hypothesized that this positively charged channel stabilizes the DNA-bound conformation by binding the R-loop and limiting reannealing of the DNA duplex. To test this hypothesis, we introduced positive-to-negative charge-swap mutations along the length of the channel. A quadruple mutant (R282E/R293D/R299E/R302E) of residues in the helical bundle of Cas8f expressed and purified similar to WT Csy complex (Figure S4). Mutations to the R-loop binding channel (RBC) result in a substantial dsDNA-binding defect (Figures 3C and S4). To confirm that this binding defect is a function of decreased R-loop stability, we repeated the experiment with a dsDNA substrate containing a non-complementary “bubble,” which would form an R-loop incapable of reannealing. Consistent with our hypothesis, the RBC mutant bound the DNA bubble with WT binding affinity, demonstrating that the positive charge in this channel plays an important role in R-loop stabilization. Together, our structural and biochemical data suggest the RBC makes sequence-independent interactions with the R-loop that inhibit reannealing of the DNA duplex.

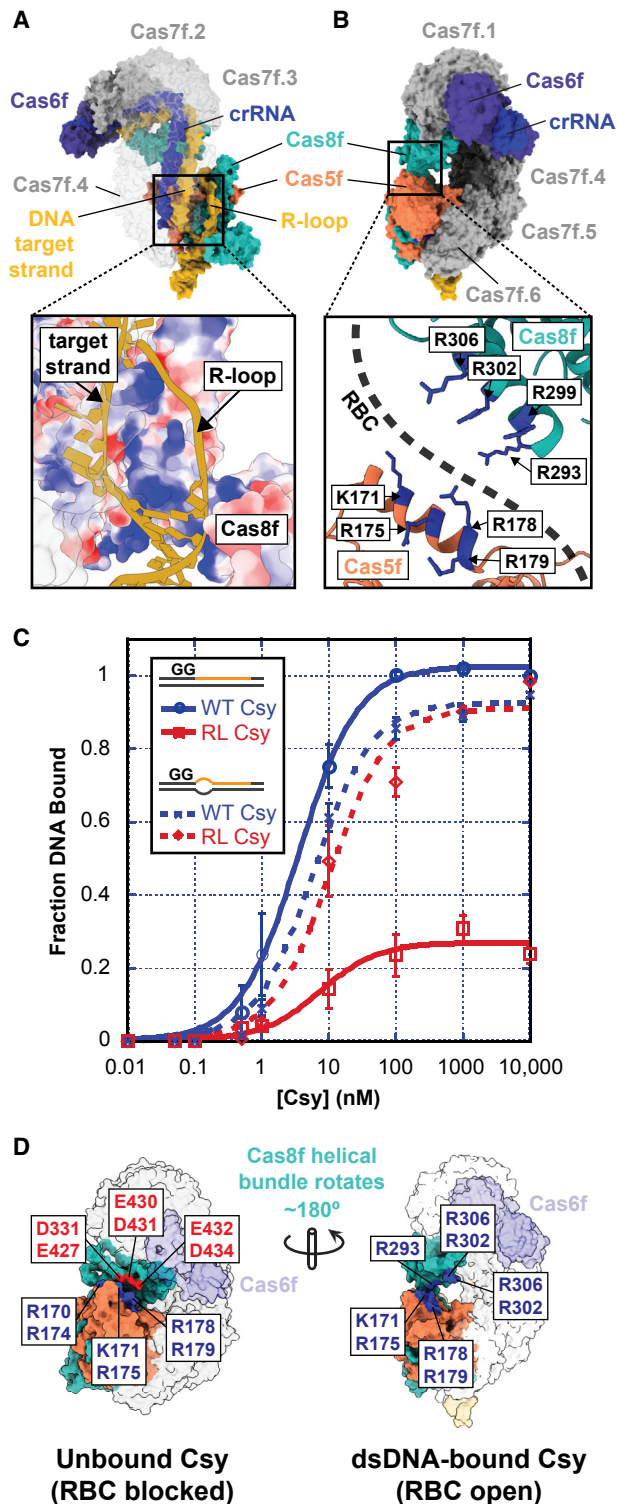


Figure 3. The Non-complementary Strand Is Positioned in a Positively Charged R-Loop Binding Channel Formed by Cas8f and Cas5f

(A) Surface representation of the dsDNA-bound Csy complex, with inset showing the non-complementary strand (R-loop) positioned in a positively charged (blue) channel formed by residues in Cas8f and Cas5f.

The PAM-distal end of the RBC is composed of arginine-rich helices on Cas5f and the helical bundle of Cas8f (Figure 3B). Notably, formation of this section of the RBC requires rotation of the Cas8f helical bundle, and rotation of the helical bundle requires dsDNA binding. When the Csy complex is unbound, the helical bundle of Cas8f is not rotated, and the Cas5f RBC helix (D166-R179) is juxtaposed with acidic residues on Cas8f (D331, E427, E430, D431, E432, and D434) (Figure 3D). In fact, this interaction between Cas5f and the unrotated Cas8f helical bundle is preserved in a structure of the Csy complex bound to dsDNA with an incomplete R-loop (Guo et al., 2017). This observation suggests R-loop binding along the length of the RBC may disrupt the charge complementation between Cas8f and Cas5f, allowing for rotation of the helical bundle.

The R-Loop Is a Regulator of Cas2/3 Recruitment

Type I-F CRISPR defense is initiated when the Csy complex binds a dsDNA target, which leads to recruitment of the *trans*-acting nuclease/helicase Cas2/3 for DNA degradation (Dwarkanath et al., 2015; Richter et al., 2014; Richter and Fineran, 2013; Rollins et al., 2015, 2017; Staals et al., 2016). However, Cas2/3 forms a complex with the adaptation protein Cas1, and Cas1 inhibits Cas2/3 nuclease activity (Fagerlund et al., 2017; Richter et al., 2014; Rollins et al., 2017). Because the Cas2/3 nuclease is activated by the DNA-bound Csy complex, we reasoned that the recruitment signal must be coincident with the conformational change that occurs during dsDNA binding. To test this hypothesis, we performed EMSAs with purified Csy complex, purified Cas1-2/3 complex, and ^{32}P -labeled dsDNAs designed to determine how specific features of the DNA ligand impact Cas2/3 recruitment. First, we measured Cas1-2/3 recruitment to Csy complex bound to a dsDNA target with a full protospacer and a GC-GC PAM, using EMSAs (Figure 4A). As previously reported, Cas1-2/3 recruitment results in two super-complexes (Rollins et al., 2017). The lower-molecular-weight complex contains dsDNA, Csy, and Cas2/3, while the larger, more transient complex that may include Cas1 (i.e., dsDNA, Csy, and Cas1-2/3). As expected, increasing concentrations of the Cas1-2/3 complex resulted in loss of the band corresponding to the dsDNA-bound Csy complex and a corresponding increase in the intensity of the bands representing dsDNA-Csy-Cas2/3 supercomplexes (Figures 4C and S5A). Next, we tested Cas2/3 recruitment to Csy complex bound to a partially duplexed target like the one used by Guo et al. (2017), whose structure

(B) Ninety-degree rotation of the DNA-bound Csy complex. Inset shows the PAM-distal end of the R-loop binding channel, formed by arginine-rich helices on Cas5f and Cas8f.

(C) Electrophoretic mobility shift assays performed with ^{32}P -labeled dsDNA substrates show that charge-swap mutations in Cas8f residues R282/R293/R299/R302 result in reduced dsDNA binding. However, high-affinity binding is rescued by DNA targets with 10-nt protospacer “bubbles.” Error bars represent SD; $n = 3$.

(D) Positions of the Cas8f and Cas5f R-loop binding channel (RBC) helices in unbound and target-bound Csy. In unbound Csy, the Cas8f RBC helix is positioned on the interior of the complex and the Cas5f RBC helix is occupied by shape and charge complementation with acidic residues on Cas8f (D331, E427, E430, D431, E432, and D434). In target-bound Csy, the Cas8f helical bundle is rotated, completing the RBC.

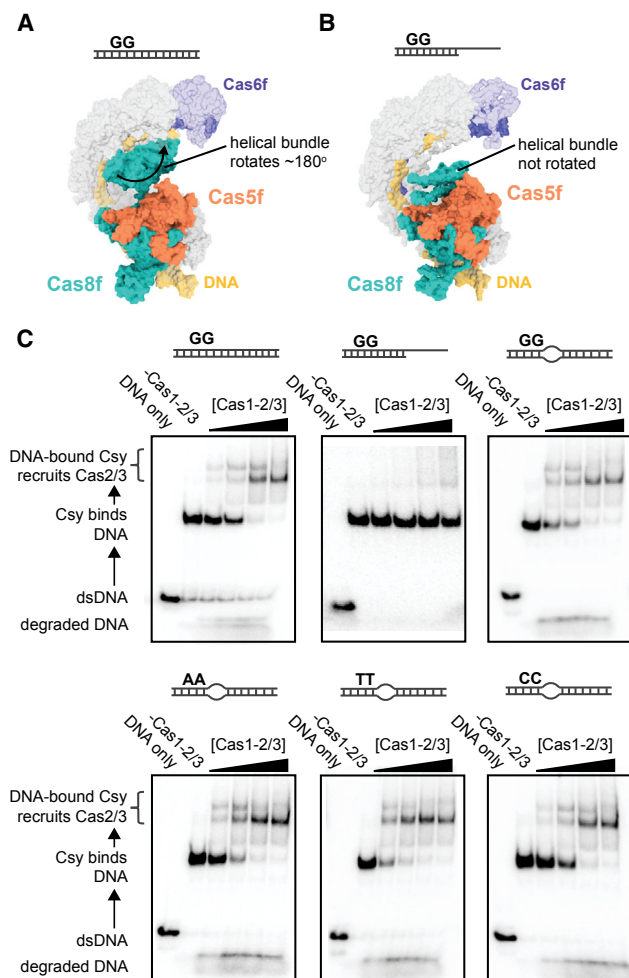


Figure 4. The R-Loop Is a Regulator of Cas2/3 Recruitment

(A) Model of the Csy complex bound to a complete dsDNA target (schematic included above). The Cas8f helical bundle is rotated $\sim 180^\circ$ relative to the unbound conformation.

(B) Model of the Csy complex bound to a partial dsDNA target (schematic included above) (PDB: 6B44). The Cas8f helical bundle is not rotated relative to the unbound conformation.

(C) Electrophoretic mobility shift assays (EMSAs) were performed with radio-labeled dsDNA substrates (illustrated schematically above each gel), purified Csy complex, and increasing concentrations (1.85 nM, 5.5 nM, 16.6 nM, or 50 nM) of the Cas1-2/3 complex. Quantification of EMSAs (Figure S5A) show a Cas1-2/3-dependent decrease in dsDNA-bound Csy complex and a corresponding increase in dsDNA-Csy-Cas2/3 supercomplex. This was seen for all DNA substrates tested except the partial duplex.

contained a closed DNA vise and an elongated Cas7f backbone but did not show a rotation of the helical bundle (Figure 4B). We hypothesized that Csy bound to this partially duplexed substrate would be unable to recruit Cas2/3, as the orientation of the Cas8f helical bundle would prevent access to the necessary docking site. Indeed, results of the EMSA experiments indicate that the partial DNA duplex does not support recruitment of the nuclease (Figure 4C). These results suggest that the R-loop is necessary for stable rotation of the helical bundle and that rotation of the helical bundle is critical for stable association with Cas2/3.

In addition to its role in target recognition, the PAM also serves as an allosteric regulator of Cas3 recruitment in type I-E systems (Hochstrasser et al., 2014; Jung et al., 2017; Xue et al., 2016). To test whether the PAM regulates Cas2/3 recruitment to the Csy complex, we performed EMSAs with targets containing a canonical double-stranded G-C/G-C PAM or a T-A/T-A, A-T/A-T, or C-G/C-G PAM (Figure 4C). The Csy complex has a stringent requirement for a PAM composed of two consecutive G-C base pairs, and PAM mutations result in severe DNA-binding defects (Rollins et al., 2015). To facilitate binding to DNA targets with mutant PAMs, we used dsDNA targets with a 10-nt bubble in the protospacer (positions 1–10) (Table S1). PAM mutants that contain the 10-nt bubble are bound with near-WT affinities, but unlike what has been reported in type I-E systems, the mutant PAMs had no effect on subsequent Cas2/3 recruitment. This suggests that the PAM in type I-F is necessary for crRNA-guided strand invasion of the DNA duplex but does not directly regulate Cas2/3 recruitment (Figure 4C).

Target-Bound Csy Complex Assumes a Locked Conformation

In addition to its role in Cas2/3 recruitment, rotation of the Cas8f helical bundle may contribute to the stable locked conformation of the dsDNA-bound Csy complex. The Csy complex stably associates with dsDNA targets that include a PAM and a complementary protospacer ($K_D \sim 1$ nM) (Chowdhury et al., 2017; Rollins et al., 2015). This binding behavior is similar to what has been reported for DNA binding by the type I-E surveillance complex (i.e., Cascade). In I-E systems, target-bound Cascade assumes a locked conformation, resulting in an extended half-life on DNA targets. Locking involves the translocation of two subunits (Cse2 proteins) that pinch the DNA target during binding (Blosser et al., 2015; Hayes et al., 2016; Rutkauskas et al., 2015; Szczelkun et al., 2014; van Erp et al., 2018; Xiao et al., 2017; Xue et al., 2016). While the type I-E and I-F surveillance complexes share morphological similarities, the I-F complex does not contain Cse2 homologs. Instead, the dsDNA-bound structure of Csy reveals an alternative locking mechanism that involves two of the six Cas7f backbone subunits (Figure 5A).

Like all other Cas7 family proteins, Cas7f proteins have a characteristic “right-hand” morphology composed of fingers-, palm-, web-, and thumb-shaped domains (Chowdhury et al., 2017). Each of these proteins “grip” the crRNA through non-sequence specific interactions with the phosphate backbone via residues distributed across each of the Cas7f domains. The thumb folds over the crRNA at regular 6-nt intervals in a way that precludes base-pairing at each of these positions. Thus, hybridization between the crRNA and the cDNA results in 5-bp segments of duplex that are interrupted at every sixth position by a thumb. The importance of the thumb in partitioning the crRNA into discrete segments has been well established, but the structure of the dsDNA-bound complex reveals that after piercing the crRNA-DNA duplex, the thumbs of Cas7f.2 and Cas7f.3 (T71-N94) curl over the top of the complementary strand and interact with the helical-bundle on Cas8f, creating a tunnel that fully encircles the complementary strand of DNA (Figures 5B and 5C). This structural conformation appears to lock the complex in a

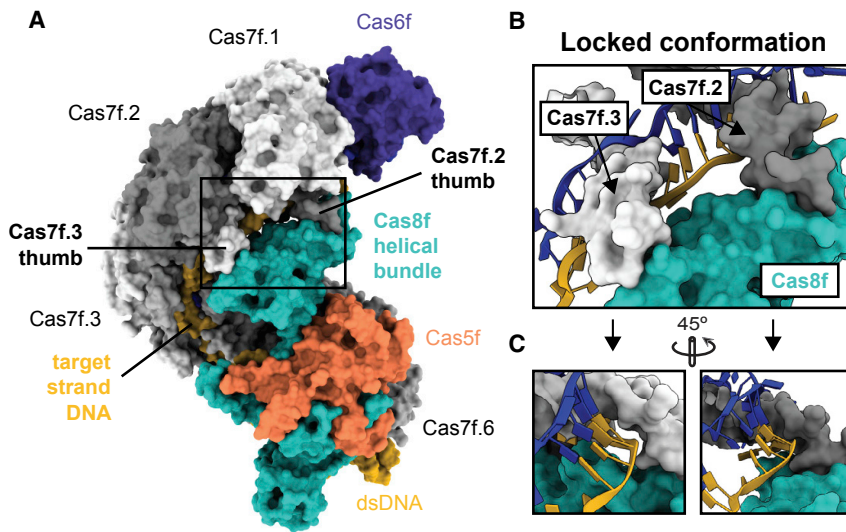


Figure 5. Target-Bound Csy Complex Adopts a Locked Conformation

(A) Surface representation of dsDNA-bound Csy complex. The target DNA strand is encapsulated by contacts between the helical bundle of Cas8f and the thumbs of Cas7f.2 and Cas7f.3.

(B) Detail of the locked conformation showing the thumbs of Cas7f.2 and Cas7f.3 (T71-N94) piercing the crRNA-DNA duplex and then folding over the top of the complementary strand and interacting with Cas8f.

(C) The cDNA strand is completely encased by the Cas7f thumbs and the helical bundle of Cas8f.

DNA-bound state and may explain the extended half-life of the target-bound Csy complex.

Anti-CRISPR AcrIF3 Is a Molecular Mimic

Bacteriophages (phages) have evolved numerous mechanisms to subvert CRISPR defense (Borges et al., 2017; Maxwell et al., 2016; Pawluk et al., 2018). Several temperate phages of *P. aeruginosa* encode small proteins that bind and neutralize type I-F Cas proteins (Bondy-Denomy et al., 2013, 2015; Borges et al., 2018; Chowdhury et al., 2017; Guo et al., 2017; Landsberger et al., 2018; Maxwell et al., 2016; Pawluk et al., 2016; Wang et al., 2016a, 2016b). One of these anti-CRISPR proteins (AcrIF3) binds Cas2/3 and prevents its recruitment to the Csy complex (Bondy-Denomy et al., 2015; Rollins et al., 2017; Wang et al., 2016a, 2016b). The structure of AcrIF3 is similar to the helical bundle of Cas8f, suggesting that this anti-CRISPR may function as a molecular mimic (Chowdhury et al., 2017; Figure 6A). When we compared structures of the two proteins, we identified one helix with conserved amino acids (Figures 6B and 6C; Video S3). Crystal structures of Cas2/3 bound by AcrIF3 indicate that conserved residues on AcrIF3 form a hydrogen-bonding network with the C-terminal domain (CTD) of Cas2/3, and mutations in these residues abolish AcrIF3 binding (Wang et al., 2016a, 2016b). We wondered whether the corresponding residues on the Cas8f helical bundle were binding Cas2/3 in a similar way.

To test this hypothesis, we made alanine point mutations in conserved residues R390, N393, and L395 (Figures 6B and 6C). The mutations result in a Cas2/3 recruitment defect (Figures 6D and S5B). This result also supports our hypothesis that AcrIF3 blocks CRISPR defense by mimicking the helical bundle of Cas8f and occupying its binding site on Cas2/3. We took advantage of this mimicry to generate a model of the DNA-Csy-Cas2/3 supercomplex. We aligned AcrIF3 with the rotated helical bundle of Cas8f to dock Cas2/3 onto the target-bound Csy complex (Figure 6E). In the resulting model, Cas2/3 contacts the Cas8f helical bundle and parts of the N-terminal region of Cas5f. In this position, the RBC directs the displaced DNA strand into the RecA

this model will help direct further investigation of Cas2/3 recruitment and supercomplex formation in the type I-F system.

DISCUSSION

Here, we describe the mechanism by which a type I-F crRNA-guided surveillance complex recognizes dsDNA and signals recruitment of the Cas2/3 nuclease-helicase to degrade a bona fide target. We determined the cryo-EM structure of the type I-F crRNA-guided surveillance complex from *P. aeruginosa* bound to a dsDNA target (Figure 1) and compared it to a recently published structure of the complex bound to a partially duplexed DNA (Guo et al., 2017). Surprisingly, we observe a major conformational difference that requires binding dsDNA, which is the biologically relevant target. We show that both the complementary and non-complementary strands of the target duplex have distinct but coordinated roles in transitioning the complex into a nuclease-ready conformation. Hybridization between the crRNA guide and the cDNA is necessary for elongation of the Cas7f backbone, while displacement of the non-complementary strand (i.e., R-loop formation) is directly involved in rotating the C-terminal helical bundle of Cas8f. These two rearrangements (i.e., elongation and rotation) are coordinated by directional unwinding of the duplex.

Rotation of the Cas8f helical bundle creates a positively charged groove between Cas8f and Cas5f that stabilizes the R-loop and inhibits reannealing of the DNA duplex (Figure 3). The rotated conformation of Cas8f is stabilized by the “thumbs” of Cas7f.2 and Cas7f.3, which fold over the cDNA target and contact the helical bundle of Cas8f, completely encasing the cDNA target (Figure 5). This conformation provides a structural explanation for the extended half-life of the Csy complex on a DNA target and also indicates that this stabilized or locked configuration can only occur after base-pairing extends to the 3' end of the crRNA guide. This locking process is conceptually similar to locking mechanisms that have been described for the type I-E systems and conformational control mechanisms that have been reported for Cas9

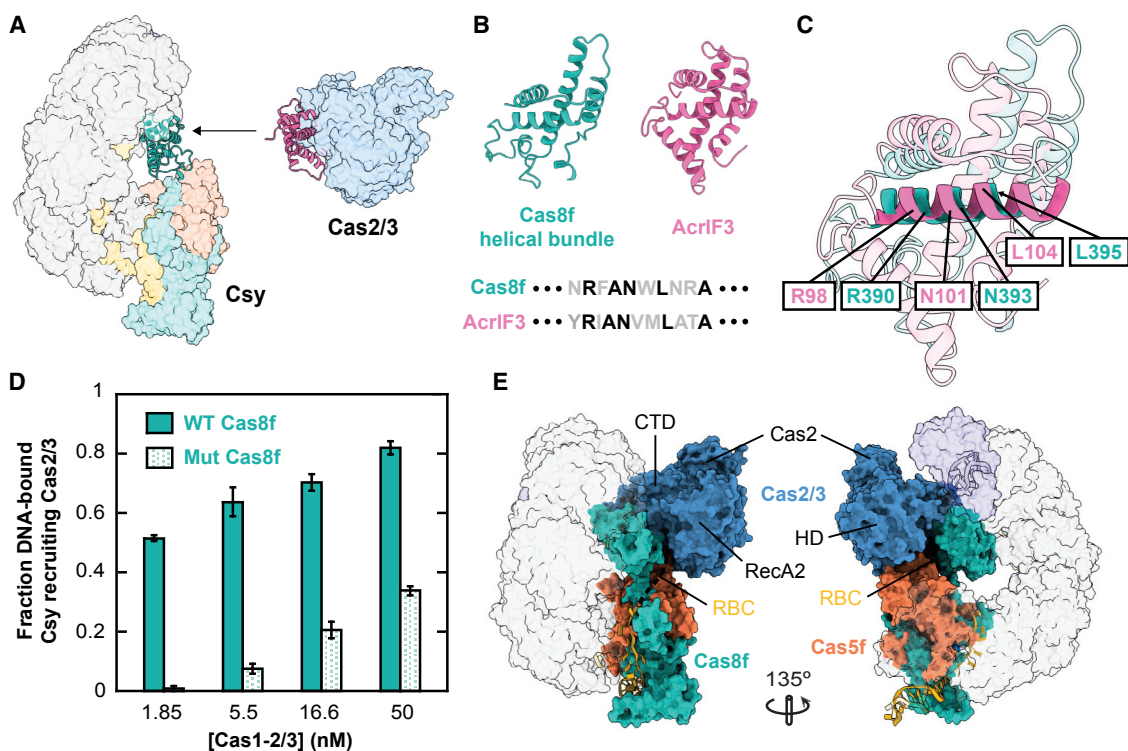


Figure 6. Anti-CRISPR Mimicry Reveals a Cas2/3 Docking Site on Csy

(A) Models of target-bound Csy complex (left) and Cas2/3 bound by the anti-CRISPR AcrIF3 (right). AcrIF3 (pink) and the helical bundle of Cas8f (green) are shown as ribbons.

(B) Structures of the Cas8f helical bundle and phage-encoded anti-CRISPR protein AcrIF3 and amino acid sequence conservation between the two proteins.

(C) Alignment of Cas8f helical bundle (green) and AcrIF3 (pink) with conserved helix in foreground. Positions of mutated residues are indicated.

(D) EMSAs were performed with radiolabeled dsDNA, purified Csy complex, and 1.85 nM, 5.5 nM, 16.6 nM, or 50 nM Cas1-2/3 complex. Quantification of Cas2/3 recruitment for WT and a triple mutation (R390A, N393A, and L395A) in Cas8f. Error bars represent SD; n = 3.

(E) Model of the dsDNA-Csy-Cas2/3 supercomplex. Cas2/3 was docked on to dsDNA-bound Csy by aligning AcrIF3 with the Cas8f helical bundle.

(Chen et al., 2017; Jackson et al., 2017; Sternberg et al., 2015; Szczelkun et al., 2014).

While coordinated movements of the Csy surveillance complex serve as a dynamic example of conformational versatility (Videos S1, S2, and S3), the biological function of the observed conformational rearrangements was not immediately evident. In particular, it was unclear if the ~180-degree rotation of the Cas8f helical bundle had functional importance beyond the locking process describe above. We previously identified structural homology between the anti-CRISPR protein AcrIF3 and this helical bundle (Chowdhury et al., 2017), and given that AcrIF3 binds Cas2/3 (Bondy-Denomy et al., 2015; Wang et al., 2016a, 2016b), we hypothesized that the helical bundle may similarly interact with Cas2/3. To test this hypothesis, we initially superimposed structures of AcrIF3 bound to Cas2/3 onto the helical bundle of Cas8f. Performing this superposition using structures of the Csy complex before DNA binding or after binding to a partially duplex DNA resulted in substantial steric clashes between Cas2/3 and the Cas7f backbone (Figure 7). However, the structure presented here shows that dsDNA binding reorients the helical bundle into a position that can accommodate Cas2/3 binding, aligning structural features of Cas2/3 with complementary features on Cas8f

and Cas5f. Moreover, the position of the Cas2/3 nuclease domain is consistent with previous biochemical data suggesting that cleavage of the R-loop occurs at the PAM-distal end of the protospacer (Rollins et al., 2017). While AcrIF3-guided docking of Cas2/3 results in a model for nuclease recruitment, we previously showed that Cas2/3 assembles with Cas1 into a heterohexamer complex. Cas1 subunits repress Cas2/3 nuclease actively until dsDNA-bound Csy recruits Cas2/3, which appears to coincide with the release of Cas1 and activation of Cas2/3 nuclease activity (Rollins et al., 2017). Since AcrIF3 also binds to the Cas1-2/3 complex, we repeated the docking experiments using Cas1-2/3, which resulted in clashing between Cas1 and the Cas8f head. This may explain how the Cas1 “repressor” is displaced from Cas2/3 upon recruitment.

Collectively, our structural and biochemical analyses not only revealed a mechanistic model for nuclease recruitment to a CRISPR-RNA-guided surveillance complex but also demonstrates how the anti-CRISPR protein AcrIF3 subverts type I-F CRISPR defense through molecular mimicry. While numerous anti-CRISPRs have now been shown to function as mimics of DNA (Chowdhury et al., 2017; Dong et al., 2017; Guo et al., 2017; Shin et al., 2017; Yang and Patel, 2017), this is the first

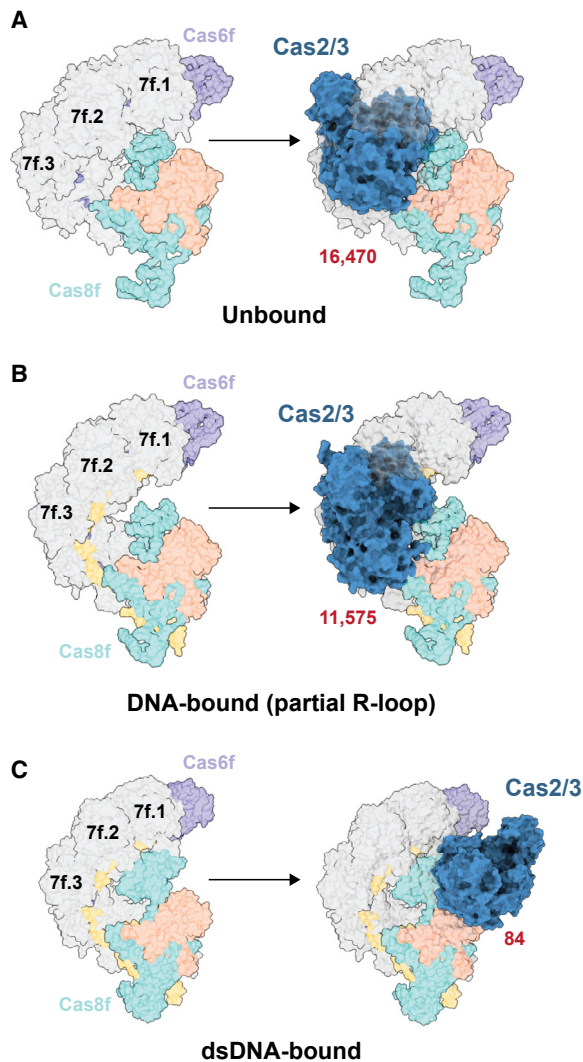


Figure 7. Double-Stranded DNA-Induced Conformational Change in Cas8f Exposes a Cas2/3 Nuclease Recruitment Helix

(A–C) Surface models of the Csy complex showing unbound Csy (A; PDB: 6B45), Csy bound to partially duplexed DNA (B; PDB: 6B44), and dsDNA-bound Csy (C; PDB: 6NE0). Cas2/3 (blue) was docked onto each model by aligning AcrIF3 with the Cas8f helical bundle. Red numbers indicate the number of clashing atoms between Cas2/3 and Csy.

example of an anti-CRISPR that mimics a Cas protein and suggests that cas genes themselves may serve as genetic fodder for the evolution of anti-CRISPR proteins. Alternatively, it is possible that structural similarity between AcrIF3 and Cas8f arose due to convergent evolution. This study emphasizes the importance of anti-CRISPRs as tools to understand the functions of CRISPR-Cas systems they target.

STAR★METHODS

Detailed methods are provided in the online version of this paper and include the following:

- **KEY RESOURCES TABLE**
- **CONTACT FOR REAGENT AND RESOURCE SHARING**
- **EXPERIMENTAL MODEL AND SUBJECT SHARING**
 - Microbes
- **METHOD DETAILS**
 - Protein expression and purification
 - Electron microscopy
 - EMSAs
- **QUANTIFICATION AND STATISTICAL ANALYSIS**
- **DATA AND SOFTWARE AVAILABILITY**

SUPPLEMENTAL INFORMATION

Supplemental Information can be found with this article online at <https://doi.org/10.1016/j.molcel.2019.02.001>.

ACKNOWLEDGMENTS

We are grateful to Bill Anderson, The Scripps Research Institute (TSRI) Electron Microscopy facility manager, and Jean-Christophe Ducom at TSRI High Performance Computing for support during EM data collection and processing. G.C.L. is supported as a Searle Scholar, a Pew Scholar, by a young investigator award from Amgen and the NIH (DP2EB020402). Research in the Wiedenheft lab is supported by the NIH (P30GM110732, R01GM110270, R01GM108888, and R21 AI130670), the National Science Foundation EPSCoR (EPS-110134), the M.J. Murdock Charitable Trust, a young investigator award from Amgen, and the Montana State University Agricultural Experimental Station (USDA NIFA). Computational analyses of EM data were performed using shared instrumentation at TSRI funded by the NIH (S10OD021634).

AUTHOR CONTRIBUTIONS

M.F.R. and S.M.G. purified the dsDNA-bound Csy complex. S.M.G. and H.M.M. performed site-directed mutagenesis. S.C. and C.M.L. performed cryo-EM. S.C. performed image analysis and reconstructions. M.F.R., S.C., and J.C. built the atomic models. M.F.R., D.F., and A.S.-F. performed the biochemical experiments. All authors contributed to analysis and interpretation of the experimental results and data. M.F.R., S.C., G.C.L., and B.W. prepared the figures; M.F.R., S.C., G.C.L., and B.W. wrote the manuscript.

DECLARATION OF INTERESTS

B.W. is the founder of SurGene, LLC, and is an inventor on patent applications related to CRISPR-Cas systems and applications thereof.

Received: October 4, 2018
 Revised: December 21, 2018
 Accepted: January 30, 2019
 Published: March 11, 2019

REFERENCES

- Adams, P.D., Afonine, P.V., Bunkoczi, G., Chen, V.B., Davis, I.W., Echols, N., Headd, J.J., Hung, L.W., Kapral, G.J., Grosse-Kunstleve, R.W., et al. (2010). PHENIX: a comprehensive Python-based system for macromolecular structure solution. *Acta Cryst* 66, 213–221.
- Afonine, P.V., Grosse-Kunstleve, R.W., Echols, N., Headd, J.J., Moriarty, N.W., Mustyakimov, M., Terwilliger, T.C., Urzhumtsev, A., Zwart, P.H., and Adams, P.D. (2012). Towards automated crystallographic structure refinement with phenix.refine. *Acta Crystallogr. D Biol. Crystallogr.* 68, 352–367.
- Bai, X.C., Rajendra, E., Yang, G., Shi, Y., and Scheres, S.H.W. (2015). Sampling the conformational space of the catalytic subunit of human γ -secretase. *eLife* 4, e11182.

- Blosser, T.R., Loeff, L., Westra, E.R., Vlot, M., Künne, T., Sobota, M., Dekker, C., Brouns, S.J.J., and Joo, C. (2015). Two distinct DNA binding modes guide dual roles of a CRISPR-Cas protein complex. *Mol. Cell* 58, 60–70.
- Bondy-Denomy, J., Pawluk, A., Maxwell, K.L., and Davidson, A.R. (2013). Bacteriophage genes that inactivate the CRISPR/Cas bacterial immune system. *Nature* 493, 429–432.
- Bondy-Denomy, J., Garcia, B., Strum, S., Du, M., Rollins, M.F., Hidalgo-Reyes, Y., Wiedenheft, B., Maxwell, K.L., and Davidson, A.R. (2015). Multiple mechanisms for CRISPR-Cas inhibition by anti-CRISPR proteins. *Nature* 526, 136–139.
- Borges, A.L., Davidson, A.R., and Bondy-Denomy, J. (2017). The discovery, mechanisms, and evolutionary impact of anti-CRISPRs. *Annu. Rev. Virol.* 4, 37–59.
- Borges, A.L., Zhang, J.Y., Rollins, M.F., Osuna, B.A., Wiedenheft, B., and Bondy-Denomy, J. (2018). Bacteriophage cooperation suppresses CRISPR-Cas3 and Cas9 immunity. *Cell* 174, 917–925.e10.
- Brouns, S.J.J., Jore, M.M., Lundgren, M., Westra, E.R., Slijkhuis, R.J.H., Snijders, A.P.L., Dickman, M.J., Makarova, K.S., Koonin, E.V., and van der Oost, J. (2008). Small CRISPR RNAs guide antiviral defense in prokaryotes. *Science* 321, 960–964.
- Chen, J.S., Dagdas, Y.S., Kleinstiver, B.P., Welch, M.M., Sousa, A.A., Harrington, L.B., Sternberg, S.H., Joung, J.K., Yildiz, A., and Doudna, J.A. (2017). Enhanced proofreading governs CRISPR-Cas9 targeting accuracy. *Nature* 550, 407–410.
- Chowdhury, S., Carter, J., Rollins, M.F., Golden, S.M., Jackson, R.N., Hoffmann, C., Nosaka, L., Bondy-Denomy, J., Maxwell, K.L., Davidson, A.R., et al. (2017). Structure reveals mechanisms of viral suppressors that intercept a CRISPR RNA-guided surveillance complex. *Cell* 169, 47–57.e11.
- Dong, D., Guo, M., Wang, S., Zhu, Y., Wang, S., Xiong, Z., Yang, J., Xu, Z., and Huang, Z. (2017). Structural basis of CRISPR-SpyCas9 inhibition by an anti-CRISPR protein. *Nature* 546, 436–439.
- Dwarakanath, S., Brenzinger, S., Gleditsch, D., Plagens, A., Klingl, A., Thormann, K., and Randau, L. (2015). Interference activity of a minimal Type I CRISPR-Cas system from *Shewanella putrefaciens*. *Nucleic Acids Res.* 43, 8913–8923.
- Emsley, P., and Cowtan, K. (2004). Coot: model-building tools for molecular graphics. *Acta Crystallogr. D Biol. Crystallogr.* 60, 2126–2132.
- Fagerlund, R.D., Wilkinson, M.E., Klykov, O., Barendregt, A., Pearce, F.G., Kieper, S.N., Maxwell, H.W.R., Capolupo, A., Heck, A.J.R., Krause, K.L., et al. (2017). Spacer capture and integration by a type I-F Cas1-Cas2-3 CRISPR adaptation complex. *Proc. Natl. Acad. Sci. USA* 114, E5122–E5128.
- Goddard, T.D., Huang, C.C., and Ferrin, T.E. (2007). Visualizing density maps with UCSF Chimera. *J. Struct. Biol.* 157, 281–287.
- Goddard, T.D., Huang, C.C., Meng, E.C., Pettersen, E.F., Couch, G.S., Morris, J.H., and Ferrin, T.E. (2018). UCSF ChimeraX: Meeting modern challenges in visualization and analysis. *Protein Sci.* 27, 14–25.
- Gong, B., Shin, M., Sun, J., Jung, C.H., Bolt, E.L., van der Oost, J., and Kim, J.S. (2014). Molecular insights into DNA interference by CRISPR-associated nuclease-helicase Cas3. *Proc. Natl. Acad. Sci. USA* 111, 16359–16364.
- Guo, T.W., Bartesaghi, A., Yang, H., Falconieri, V., Rao, P., Merk, A., Eng, E.T., Raczowski, A.M., Fox, T., Earl, L.A., et al. (2017). Cryo-EM structures reveal mechanism and inhibition of DNA targeting by a CRISPR-Cas surveillance complex. *Cell* 171, 414–426.e412.
- Haurwitz, R.E., Jinek, M., Wiedenheft, B., Zhou, K., and Doudna, J.A. (2010). Sequence- and structure-specific RNA processing by a CRISPR endonuclease. *Science* 329, 1355–1358.
- Hayes, R.P., Xiao, Y., Ding, F., van Erp, P.B., Rajashankar, K., Bailey, S., Wiedenheft, B., and Ke, A. (2016). Structural basis for promiscuous PAM recognition in type I-E Cascade from *E. coli*. *Nature* 530, 499–503.
- Herzik, M.A., Jr., Fraser, J.S., and Lander, G.C. (2019). A multi-model approach to assessing local and global cryo-EM map quality. *Structure* 27, 344–358.e3.
- Heymann, J.B., and Belnap, D.M. (2007). Bsoft: image processing and molecular modeling for electron microscopy. *J. Struct. Biol.* 157, 3–18.
- Hille, F., Richter, H., Wong, S.P., Bratović, M., Ressel, S., and Charpentier, E. (2018). The Biology of CRISPR-Cas: Backward and Forward. *Cell* 172, 1239–1259.
- Hochstrasser, M.L., Taylor, D.W., Bhat, P., Guegler, C.K., Sternberg, S.H., Nogales, E., and Doudna, J.A. (2014). CasA mediates Cas3-catalyzed target degradation during CRISPR RNA-guided interference. *Proc. Natl. Acad. Sci. USA* 111, 6618–6623.
- Hochstrasser, M.L., Taylor, D.W., Kornfeld, J.E., Nogales, E., and Doudna, J.A. (2016). DNA targeting by a minimal CRISPR RNA-guided Cascade. *Mol. Cell* 63, 840–851.
- Huo, Y., Nam, K.H., Ding, F., Lee, H., Wu, L., Xiao, Y., Farchione, M.D., Jr., Zhou, S., Rajashankar, K., Kurinov, I., et al. (2014). Structures of CRISPR Cas3 offer mechanistic insights into Cascade-activated DNA unwinding and degradation. *Nat. Struct. Mol. Biol.* 21, 771–777.
- Jackson, R.N., and Wiedenheft, B. (2015). A conserved structural chassis for mounting versatile CRISPR RNA-guided immune responses. *Mol. Cell* 58, 722–728.
- Jackson, R.N., Lavin, M., Carter, J., and Wiedenheft, B. (2014). Fitting CRISPR-associated Cas3 into the helicase family tree. *Curr. Opin. Struct. Biol.* 24, 106–114.
- Jackson, R.N., van Erp, P.B., Sternberg, S.H., and Wiedenheft, B. (2017). Conformational regulation of CRISPR-associated nucleases. *Curr. Opin. Microbiol.* 37, 110–119.
- Jung, C., Hawkins, J.A., Jones, S.K., Jr., Xiao, Y., Rybarski, J.R., Dillard, K.E., Hussmann, J., Saifuddin, F.A., Savran, C.A., Ellington, A.D., et al. (2017). Massively parallel biophysical analysis of CRISPR-Cas complexes on next generation sequencing chips. *Cell* 170, 35–47.e13.
- Kimanius, D., Forsberg, B.O., Scheres, S.H., and Lindahl, E. (2016). Accelerated cryo-EM structure determination with parallelisation using GPUs in RELION-2. *eLife* 5, e18722.
- Koonin, E.V., Makarova, K.S., and Zhang, F. (2017). Diversity, classification and evolution of CRISPR-Cas systems. *Curr. Opin. Microbiol.* 37, 67–78.
- Lander, G.C., Stagg, S.M., Voss, N.R., Cheng, A., Fellmann, D., Pulokas, J., Yoshioka, C., Irving, C., Mulder, A., Lau, P.W., et al. (2009). Appion: an integrated, database-driven pipeline to facilitate EM image processing. *J. Struct. Biol.* 166, 95–102.
- Landsberger, M., Gandon, S., Meaden, S., Rollie, C., Chevallereau, A., Chabas, H., Buckling, A., Westra, E.R., and van Houte, S. (2018). Anti-CRISPR phages cooperate to overcome CRISPR-Cas immunity. *Cell* 174, 908–916.e12.
- Leenay, R.T., Maksimchuk, K.R., Slotkowski, R.A., Agrawal, R.N., Gomia, A.A., Briner, A.E., Barrangou, R., and Beisel, C.L. (2016). Identifying and visualizing functional PAM diversity across CRISPR-Cas systems. *Mol. Cell* 62, 137–147.
- Loeff, L., Brouns, S.J.J., and Joo, C. (2018). Repetitive DNA reeling by the Cascade-Cas3 complex in nucleotide unwinding steps. *Mol. Cell* 70, 385–394.e3.
- Makarova, K.S., Wolf, Y.I., Alkhnbashi, O.S., Costa, F., Shah, S.A., Saunders, S.J., Barrangou, R., Brouns, S.J., Charpentier, E., Haft, D.H., et al. (2015). An updated evolutionary classification of CRISPR-Cas systems. *Nat. Rev. Microbiol.* 13, 722–736.
- Marraffini, L.A. (2015). CRISPR-Cas immunity in prokaryotes. *Nature* 526, 55–61.
- Maxwell, K.L., Garcia, B., Bondy-Denomy, J., Bona, D., Hidalgo-Reyes, Y., and Davidson, A.R. (2016). The solution structure of an anti-CRISPR protein. *Nat. Commun.* 7, 13134.
- Mohanraju, P., Makarova, K.S., Zetsche, B., Zhang, F., Koonin, E.V., and van der Oost, J. (2016). Diverse evolutionary roots and mechanistic variations of the CRISPR-Cas systems. *Science* 353, aad5147.
- Mojica, F.J., Diez-Villaseñor, C., García-Martínez, J., and Almendros, C. (2009). Short motif sequences determine the targets of the prokaryotic CRISPR defence system. *Microbiology* 155, 733–740.
- Mulepati, S., and Bailey, S. (2013). In vitro reconstitution of an *Escherichia coli* RNA-guided immune system reveals unidirectional, ATP-dependent degradation of DNA target. *J. Biol. Chem.* 288, 22184–22192.

- Murugan, K., Babu, K., Sundaresan, R., Rajan, R., and Sashital, D.G. (2017). The revolution continues: newly discovered systems expand the CRISPR-Cas toolkit. *Mol. Cell* **68**, 15–25.
- Pausch, P., Muller-Esparza, H., Gleditsch, D., Altegoer, F., Randau, L., and Bange, G. (2017). Structural variation of type I-F CRISPR RNA guided DNA surveillance. *Mol. Cell* **67**, 622–632.e624.
- Pawluk, A., Staals, R.H., Taylor, C., Watson, B.N., Saha, S., Fineran, P.C., Maxwell, K.L., and Davidson, A.R. (2016). Inactivation of CRISPR-Cas systems by anti-CRISPR proteins in diverse bacterial species. *Nat. Microbiol.* **1**, 16085.
- Pawluk, A., Davidson, A.R., and Maxwell, K.L. (2018). Anti-CRISPR: discovery, mechanism and function. *Nat. Rev. Microbiol.* **16**, 12–17.
- Peng, R., Xu, Y., Zhu, T., Li, N., Qi, J., Chai, Y., Wu, M., Zhang, X., Shi, Y., Wang, P., et al. (2017). Alternate binding modes of anti-CRISPR viral suppressors AcrF1/2 to Csy surveillance complex revealed by cryo-EM structures. *Cell Res.* **27**, 853–864.
- Przybilski, R., Richter, C., Gristwood, T., Clulow, J.S., Vercoe, R.B., and Fineran, P.C. (2011). Csy4 is responsible for CRISPR RNA processing in *Pectobacterium atrosepticum*. *RNA Biol.* **8**, 517–528.
- Redding, S., Sternberg, S.H., Marshall, M., Gibb, B., Bhat, P., Guegler, C.K., Wiedenheft, B., Doudna, J.A., and Greene, E.C. (2015). Surveillance and processing of foreign DNA by the *Escherichia coli* CRISPR-Cas system. *Cell* **163**, 854–865.
- Richter, C., and Fineran, P.C. (2013). The subtype I-F CRISPR-Cas system influences pathogenicity island retention in *Pectobacterium atrosepticum* via crRNA generation and Csy complex formation. *Biochem. Soc. Trans.* **41**, 1468–1474.
- Richter, C., Gristwood, T., Clulow, J.S., and Fineran, P.C. (2012). In vivo protein interactions and complex formation in the *Pectobacterium atrosepticum* subtype I-F CRISPR/Cas System. *PLoS ONE* **7**, e49549.
- Richter, C., Dy, R.L., McKenzie, R.E., Watson, B.N., Taylor, C., Chang, J.T., McNeil, M.B., Staals, R.H., and Fineran, P.C. (2014). Priming in the Type I-F CRISPR-Cas system triggers strand-independent spacer acquisition, bi-directionally from the primed protospacer. *Nucleic Acids Res.* **42**, 8516–8526.
- Rohou, A., and Grigorieff, N. (2015). CTFIND4: fast and accurate defocus estimation from electron micrographs. *J. Struct. Biol.* **192**, 216–221.
- Rollins, M.F., Schuman, J.T., Paulus, K., Bukhari, H.S., and Wiedenheft, B. (2015). Mechanism of foreign DNA recognition by a CRISPR RNA-guided surveillance complex from *Pseudomonas aeruginosa*. *Nucleic Acids Res.* **43**, 2216–2222.
- Rollins, M.F., Chowdhury, S., Carter, J., Golden, S.M., Wilkinson, R.A., Bondy-Denomy, J., Lander, G.C., and Wiedenheft, B. (2017). Cas1 and the Csy complex are opposing regulators of Cas2/3 nuclease activity. *Proc. Natl. Acad. Sci. USA* **114**, E5113–E5121.
- Roseman, A.M. (2004). FindEm—a fast, efficient program for automatic selection of particles from electron micrographs. *J. Struct. Biol.* **145**, 91–99.
- Rutkauskas, M., Sinkunas, T., Songailiene, I., Tikhomirova, M.S., Siksnys, V., and Seidel, R. (2015). Directional R-loop formation by the CRISPR-Cas surveillance complex Cascade provides efficient off-target site rejection. *Cell Rep.* **10**, P1534–P1543.
- Shin, J., Jiang, F., Liu, J.J., Bray, N.L., Rauch, B.J., Baik, S.H., Nogales, E., Bondy-Denomy, J., Corn, J.E., and Doudna, J.A. (2017). Disabling Cas9 by an anti-CRISPR DNA mimic. *Sci. Adv.* **3**, e1701620.
- Shmakov, S., Smargon, A., Scott, D., Cox, D., Pyzocha, N., Yan, W., Abudayyeh, O.O., Gootenberg, J.S., Makarova, K.S., Wolf, Y.I., et al. (2017). Diversity and evolution of class 2 CRISPR-Cas systems. *Nat. Rev. Microbiol.* **15**, 169–182.
- Sinkunas, T., Gasiunas, G., Fremaux, C., Barrangou, R., Horvath, P., and Siksnys, V. (2011). Cas3 is a single-stranded DNA nuclease and ATP-dependent helicase in the CRISPR/Cas immune system. *EMBO J.* **30**, 1335–1342.
- Sorzano, C.O., Marabini, R., Velasquez-Muriel, J., Bilbao-Castro, J.R., Scheres, S.H., Carazo, J.M., and Pascual-Montano, A. (2004). XMIPP: a new generation of an open-source image processing package for electron microscopy. *J. Struct. Biol.* **148**, 194–204.
- Staals, R.H., Jackson, S.A., Biswas, A., Brouns, S.J., Brown, C.M., and Fineran, P.C. (2016). Interference-driven spacer acquisition is dominant over naive and primed adaptation in a native CRISPR-Cas system. *Nat. Commun.* **7**, 12853.
- Sternberg, S.H., Haurwitz, R.E., and Doudna, J.A. (2012). Mechanism of substrate selection by a highly specific CRISPR endoribonuclease. *RNA* **18**, 661–672.
- Sternberg, S.H., LaFrance, B., Kaplan, M., and Doudna, J.A. (2015). Conformational control of DNA target cleavage by CRISPR-Cas9. *Nature* **527**, 110–113.
- Suloway, C., Pulokas, J., Fellmann, D., Cheng, A., Guerra, F., Quispe, J., Stagg, S., Potter, C.S., and Carragher, B. (2005). Automated molecular microscopy: the new Leginon system. *J. Struct. Biol.* **157**, 41–60.
- Szczelkun, M.D., Tikhomirova, M.S., Sinkunas, T., Gasiunas, G., Karvelis, T., Pschera, P., Siksnys, V., and Seidel, R. (2014). Direct observation of R-loop formation by single RNA-guided Cas9 and Cascade effector complexes. *Proc. Natl. Acad. Sci. USA* **111**, 9798–9803.
- van Erp, P.B.G., Patterson, A., Kant, R., Berry, L., Golden, S.M., Forsman, B.L., Carter, J., Jackson, R.N., Bothner, B., and Wiedenheft, B. (2018). Conformational dynamics of DNA binding and Cas3 recruitment by the CRISPR RNA-guided Cascade complex. *ACS Chem. Biol.* **13**, 481–490.
- van Houte, S., Buckling, A., and Westra, E.R. (2016). Evolutionary ecology of prokaryotic immune mechanisms. *Microbiol. Mol. Biol. Rev.* **80**, 745–763.
- Voss, N.R., Yoshioka, C.K., Radermacher, M., Potter, C.S., and Carragher, B. (2009). DoG Picker and TiltPicker: software tools to facilitate particle selection in single particle electron microscopy. *J. Struct. Biol.* **166**, 205–213.
- Wang, J., Ma, J., Cheng, Z., Meng, X., You, L., Wang, M., Zhang, X., and Wang, Y. (2016a). A CRISPR evolutionary arms race: structural insights into viral anti-CRISPR/Cas responses. *Cell Res.* **26**, 1165–1168.
- Wang, X., Yao, D., Xu, J.G., Li, A.R., Xu, J., Fu, P., Zhou, Y., and Zhu, Y. (2016b). Structural basis of Cas3 inhibition by the bacteriophage protein AcrF3. *Nat. Struct. Mol. Biol.* **23**, 868–870.
- Westra, E.R., van Erp, P.B., Künne, T., Wong, S.P., Staals, R.H., Seegers, C.L., Bollen, S., Jore, M.M., Semenova, E., Severinov, K., et al. (2012). CRISPR immunity relies on the consecutive binding and degradation of negatively supercoiled invader DNA by Cascade and Cas3. *Mol. Cell* **46**, 595–605.
- Wiedenheft, B., van Duijn, E., Bultema, J.B., Waghmare, S.P., Zhou, K., Barendregt, A., Westphal, W., Heck, A.J., Boekema, E.J., Dickman, M.J., and Doudna, J.A. (2011). RNA-guided complex from a bacterial immune system enhances target recognition through seed sequence interactions. *Proc. Natl. Acad. Sci. USA* **108**, 10092–10097.
- Wilkinson, R., and Wiedenheft, B. (2014). A CRISPR method for genome engineering. *F1000Prime Rep.* **6**, 3.
- Xiao, Y., Luo, M., Hayes, R.P., Kim, J., Ng, S., Ding, F., Liao, M., and Ke, A. (2017). Structure basis for directional R-loop formation and substrate hand-over mechanisms in type I CRISPR-Cas system. *Cell* **170**, 48–60.e11.
- Xue, C., Whittis, N.R., and Sashital, D.G. (2016). Conformational control of Cascade interference and priming activities in CRISPR immunity. *Mol. Cell* **64**, 826–834.
- Xue, C., Zhu, Y., Zhang, X., Shin, Y.K., and Sashital, D.G. (2017). Real-time observation of target search by the CRISPR surveillance complex Cascade. *Cell Rep.* **21**, 3717–3727.
- Yang, H., and Patel, D.J. (2017). Inhibition mechanism of an anti-CRISPR suppressor AcrIIA4 targeting SpyCas9. *Mol. Cell* **67**, 117–127.e115.
- Zheng, S.Q., Palovcak, E., Armache, J.P., Verba, K.A., Cheng, Y., and Agard, D.A. (2017). MotionCorr2: anisotropic correction of beam-induced motion for improved cryo-electron microscopy. *Nat. Methods* **14**, 331–332.

STAR★METHODS

KEY RESOURCES TABLE

REAGENT or Resource	SOURCE	IDENTIFIER
Bacterial and virus strains		
<i>E. coli</i> : Bl21 DE3 competent cells	NEB	Cat# C25271
<i>E. coli</i> : Bl21 DH5 α competent cells	ThermoFisher	Cat# 18265017
Chemicals, Peptides, and Recombinant Proteins		
TCEP	Soltec	Cat# M115
LMNG	Anatrace	Cat# NG310 1 GM
Protease inhibitor cocktail	Thermo Scientific	Cat# 1861278
T4 DNA ligase	NEB	Cat# M0202S
PNK	NEB	Cat# M0201s
DPN I	NEB	Cat# R0176s
³² P-ATP	Perkin Elmer	Cat# 100539131
Deposited Data		
Structure of Csy complex bound to dsDNA	This paper	PDB: 6NE0
Structure of Csy complex bound to dsDNA	This paper	EMDB: 9191
pCsy_complex expression vector	Wiedenheft lab	Addgene plasmid # 89232
pCRISPR_DMS3g24 expression vector	Wiedenheft lab	Addgene plasmid # 89244
pCas1-2/3 expression vector	Wiedenheft lab	Addgene plasmid #89230
Unprocessed gel images		https://data.mendeley.com/datasets/63ntskx3fw/2
Oligonucleotides		
Primer: Cas8f_N250A.F: CAAGCCGCAGgccATCAGTCAGTTG	Eurofins	n/a
Primer: Cas8f_N250A.R: GTACCGCCGAACTTCTGG	Eurofins	n/a
Primer: Cas8f_R282E/H283D.F: CGCGCCGATGGAAGACTCTTCGGTCT	Eurofins	n/a
Primer: Cas8f_R282E/H283D.R: TTTACATTCTGCCTTTGCC	Eurofins	n/a
Primer: Cas8f_R299E/R302E.F: ACCGAAACCCTGCAGCGTTTTCTT	Eurofins	n/a
Primer: Cas8f_R299E/R302E.R: TAGTTCGGATACTTCAGGAGTTCTTCC	Eurofins	n/a
Primer: Cas8f_R390A/N393A/L395A.F: GGCGAACCGGGCGGTCAGCAG	Eurofins	n/a
Primer: Cas8f_R390A/N393A/L395A.R: CAGGCGGCGAACGCATTTCCGACC	Eurofins	n/a
Oligonucleotides for gel shift: 80-bp target with GG PAM GCTGTACGTCACTATCGAAGCAATACAGGTAGACGCGGAC ATCAAGCCCGCCGTGAAGGTGCAGCTTCTCTACAGAGTGC	Eurofins	n/a
Oligonucleotides for gel shift: 80-bp non-target with GG PAM GCACTCTGTAGAGAAGCTGCACCTTACGCGGGCTTGAT GTCCGCGTCTACCTGTATTGCTTCGATAGTGACGTACAGC	Eurofins	n/a
Oligonucleotides for gel shift: 80-bp target with GG PAM, bubble in positions +1 - +10 GCTGTACGTCACTATCGAAGC AATACAGGTAGACGCGGACATCAAGCCCGCCGTGAAGGT GCAGCTTCTCTACAGAGTGC	Eurofins	n/a
Oligonucleotides for gel shift: 80-bp non-target with GG PAM, bubble in positions +1 - +10 GCACTCTGTAGAGAAGCTGCA CCAAGTGCCGCGCTTGATGTCCGCGTCTACCTGTATTGC TTCGATAGTGACGTACAGC	Eurofins	n/a

(Continued on next page)

Continued

REAGENT or Resource	SOURCE	IDENTIFIER
Oligonucleotides for gel shift: 80-bp target with TT PAM, bubble in positions +1 - +10 GCTGTACGTCACCTATCGAAGCAATACAGG TAGACGCGGACATCAAGCCCGCCGTGAATTTGCAGCTTCTCT ACAGAGTGC	Eurofins	n/a
Oligonucleotides for gel shift: 80-bp non-target with TT PAM, bubble in positions +1 - +10 GCACTCTGTAGAGAAGCTGCA AAAAGTGCCGCGCTTGATGTCCGCGTCTACCTGTATTGC TTCGATAGTGACGTACAGC	Eurofins	n/a
Oligonucleotides for gel shift: 80-bp target with AA PAM, bubble in positions +1 - +10 GCTGTACGTCACCTATCGAAGCAATACAGG TAGACGCGGACATCAAGCCCGCCGTGAAAATGCAGCTTCTCT ACAGAGTGC	Eurofins	n/a
Oligonucleotides for gel shift: 80-bp non-target with AA PAM, bubble in positions +1 - +10 GCACTCTGTAGAGAAGCTGCATTAA GTGCCGCGCTTGATGTCCGCGTCTACCTGTATTGCTTCGATAG TGACGTACAGC	Eurofins	n/a
Oligonucleotides for gel shift: 80-bp target with CC PAM, bubble in positions +1 - +10 GCTGTACGTCACCTATCGAAGCAATACAGG AGACGCGGACATCAAGCCCGCCGTGAACCTGCAGCTTCTCTAC AGAGTGC	Eurofins	n/a
Oligonucleotides for gel shift: 80-bp non-target with CC PAM, bubble in positions +1 - +10 GCACTCTGTAGAGAAGCTGCAGGAA GTGCCGCGCTTGATGTCCGCGTCTACCTGTATTGCTTCGATAG TGACGTACAGC	Eurofins	n/a
Oligonucleotides for gel shift: partial non-target strand to pair with 80bp target strand with GG PAM GCACTCTGTAGAGAAGCTGCA CCTTCACGGCGG	Eurofins	n/a
Recombinant DNA		
Plasmid: pCsy_complex	Wiedenheft lab	Addgene plasmid # 89232
Plasmid: pCsy_complex Cas8f K247E	Chowdhury et al., 2017	n/a
Plasmid: pCsy_complex Cas8f N250A	This study	n/a
Plasmid: pCsy_complex Cas8f R282E/H283D/R299E/R302E	This study	n/a
Plasmid: pCsy_complex Cas8f R390A/N393A/L395A	This study	n/a
Plasmid: pCas1-2/3	Wiedenheft lab	Addgene plasmid # 89230
Plasmid: pCRISPR_DMS3g24	Wiedenheft lab	Addgene plasmid # 89232
Software and Algorithms		
ImageQuant software	GE	n/a
Leginon automated software	NRAMM, NYSBC	http://emg.nysbc.org/redmine/projects/legion/wiki/Leginon_Homepage
CTFFind4	Rhou and Grigorieff, 2015	http://grigoriefflab.janelia.org/ctf
Coot	Emsley and Cowtan, 2004	https://www2.mrc-lmb.cam.ac.uk/personal/pemsley/coot/
PHENIX v1.14-3260	Adams et al., 2010	https://www.phenix-online.org/
USCF Chimera	Goddard et al., 2007	https://www.cgl.ucsf.edu/chimera/
DoG picker	Voss et al., 2009	http://emg.nysbc.org/redmine/projects/software/wiki/DoGpicker
XMIPP	Sorzano et al., 2004	https://github.com/l2PC/xmipp
RELION v2	Kimanius et al., 2016	https://www2.mrc-lmb.cam.ac.uk/relion/index.php?title=Main_Page
FindEM	Roseman, 2004	http://www.ccpem.ac.uk/download.php
ChimeraX	Goddard et al., 2018	https://www.rbvi.ucsf.edu/chimerax/

(Continued on next page)

Continued

REAGENT or Resource	SOURCE	IDENTIFIER
Other		
Spin concentrators	Corning	Cat# 431491
Ni NTA superflow column	QIAGEN	Cat# 30760
Superdex 200 HiLoad 26/600	GE	Cat# 28-9893-36
G-25 spin columns	GE	Cat# 27-5325-01
UltrAuFoil Holey Gold Films (1.2 μ m holes and 1.3 μ m spacing)	Quantifoil Micro Tools GmbH	Cat# N1-A14nAu30-01

CONTACT FOR REAGENT AND RESOURCE SHARING

Requests for materials should be addressed to Blake Wiedenheft (bwiedenheft@gmail.com).

EXPERIMENTAL MODEL AND SUBJECT SHARING**Microbes**

Escherichia coli cells were cultured on LB medium.

METHOD DETAILS**Protein expression and purification*****P. aeruginosa* Csy complex**

Csy genes and a synthetic CRISPR were co-expressed on separate vectors in *E. coli* BL21 (DE3) cells as previously described (Rollins et al., 2017). Expression was induced with 0.5 mM isopropyl-D-1-thiogalactopyranoside (IPTG) at an optical density (OD_{600nm}) ~0.5. Cells were incubated overnight at 16°C, then pelleted by centrifugation (5000 x g for 15 min at 4°C) and re-suspended in lysis buffer (50 mM 4-(2-hydroxyethyl)-1-piperazineethanesulfonic acid (HEPES) pH 7.5, 300 mM potassium chloride, 5% glycerol, 1 mM Tris(2-carboxyethyl) phosphine hydrochloride (TCEP), 1x protease inhibitor cocktail (Thermo Scientific)). Pellets were sonicated on ice for 3 x 2.5 min (1 s on, 3 s off), then lysate was clarified by centrifugation at 22,000 x g for 30 min at 4°C. The Csy complex self-assembles *in vivo* and the intact complex (with N-terminal 6-histidine affinity tags on Cas7f) was affinity purified over NiNTA resin (QIAGEN) which was washed once with lysis buffer supplemented with 20 mM imidazole before elution with lysis buffer supplemented with 300 mM imidazole. Protein was then concentrated (Corning Spin-X concentrators) at 4°C before further purification over a Superdex 200 size-exclusion column (GE Healthcare) in 20 mM HEPES pH 7.5, 100 mM KCl, 5% glycerol, 1 mM TCEP.

***P. aeruginosa* Cas1-2/3 complex**

The Cas1-2/3 complex was expressed and purified using previously described methods and the plasmids are available on Addgene (#89240) (Rollins et al., 2017). Briefly, the expression vector was transformed into *E. coli* BL21 (DE3) cells, and the cells were induced with IPTG at an OD₆₀₀ of 0.5. Expression was induced with 0.5 mM IPTG at OD₆₀₀ = 0.5 nm. Cells were pelleted and lysed as described above. Co-expressed Cas1 (with N-terminal 6-histidine affinity tag) and Cas2/3 (untagged) were affinity purified using NiNTA resin (QIAGEN), which was washed once with lysis buffer supplemented with 20 mM imidazole before elution with lysis buffer supplemented with 300 mM imidazole. Protein was concentrated (Corning Spin-X concentrators) at 4°C before further purification over a Superdex 200 size-exclusion column (GE Healthcare) in 20 mM HEPES pH 7.5, 100 mM KCl, 5% glycerol.

Electron microscopy**Grid preparation for cryo-EM**

Prior cryo-EM studies with the Csy-Acr complex (Chowdhury et al., 2017) showed that Csy complexes adopt a preferred orientation in ice. Addition of 0.05% (v/v) Lauryl Maltose Neopentyl Glycol (LMNG, Anatrace) to the sample helped in overcoming this orientation bias problem. 4 μ L of 2 mg/mL purified Csy-DNA complex, mixed with 0.05% (v/v) LMNG was added onto freshly plasma cleaned (hydrogen, oxygen plasma) 300 mesh UltrAuFoil R1.2/1.3 holey Gold grid (Quantifoil). After manually blotting off excess sample with a Whatman No.1 filter paper for 5-7 s, the sample was immediately vitrified by plunge freezing in liquid-ethane at -179°C. The entire cryo grid preparation process was carried out at 4°C and 98% relative humidity to minimize excessive evaporation of sample from grid surface.

cryo-EM data acquisition

Cryo grids were loaded into a 200keV Talos Arctica (Thermo Fisher) transmission electron microscope. 3,208 micrographs (Figure S1A) were acquired with a K2 Summit (Gatan) direct electron detector operating in super-resolution mode, using the Leginon automated data collection software (Suloway et al., 2005) at a nominal magnification of 36,000X (super-resolution pixel size of 0.575 Å/pixel; physical pixel size of 1.15 Å/pixel). Each micrograph was collected as dose-fractionated movie, where each movie

comprised of 56 frames acquired over 14 s with a cumulative exposure of ~ 58 electrons/ \AA^2 . A nominal defocus range of 0.6 μm to 1.5 μm was used for collecting the data.

Image processing and 3D reconstruction

The super-resolution movie frames were first Fourier-binned 2×2 times to a pixel size of 1.15 $\text{\AA}/\text{pixel}$, prior to dose-weighted frame alignment using MotionCor2 (Zheng et al., 2017) implemented in the Appion (Lander et al., 2009) image processing workflow. CTF parameters for the summed aligned micrographs were estimated using CTFFind4 (Rohou and Grigorieff, 2015) (Figure S1B) and only micrographs with confidence values above 90% were further processed. Particles were picked from these micrographs using the FindEM (Roseman, 2004) template-based particle picker in the Appion workflow, using selected 2D class averages from the previous Csy-Acr complex dataset as templates (Chowdhury et al., 2017). Coordinates from these picks were then imported into RELION 2.0 (Kimanius et al., 2016), and 1,543,677 particles were extracted with a box size of 288 pixels, which were binned by a factor of 2 (resulting box size 144 pixels, pixel size of 2.3 $\text{\AA}/\text{pixel}$). These particles were then subjected to reference-free 2D classification (Figure S1C) within RELION 2.0, and a stack of 962,677 particles was obtained by selecting classes that represented different orientations and contained high-resolution features. These selected particles were subjected to 3D refinement (Figure S2A), using a 60 \AA low passed filtered Csy-Acr map (EMD-8624) as an initial model. Particles from the 3D refinement were subjected to 3D classification without alignment and sorted into four classes. 743,861 particles belonging to two well-resolved 3D classes with the intact Cas8f C-terminal helix bundle were selected for further processing. Based on the x and y shifts associated with these particles, unbinned particles (box size 288 pixels, and pixel size of 1.15 $\text{\AA}/\text{pixel}$) were extracted with re-centered coordinates. These particles were subjected to unmasked 3D refinement followed by another round of refinement with a soft edged 3D binary mask. The mask used for the refinement was generated using the volume from unmasked refinement run, that was expanded by 5 pixels with 8 pixels Gaussian fall-off smoothing. All subsequent masks that were used for downstream data processing were generated using the same procedure. The resulting reconstruction reported a resolution of 3.85 \AA at a Fourier Shell Correlation (FSC) of 0.143. To further sort structural heterogeneity, particles from this 3D refinement were subjected to three class 3D classification without alignment. 291,227 particles from the best resolved 3D class of the full complex (containing the helix bundle of Cas8f) were further refined, resulting in a 3.4 \AA resolution (at an FSC of 0.143) reconstruction (Figure S3G). Though the majority of this reconstruction presented well-defined structural details, the head, tail, and the helix bundle region of the Csy-DNA complex were poorly resolved due to intrinsic flexibility (Figures S2A and S2C).

In order to improve the quality of the map for the different regions of the Csy-DNA complex we used the signal-subtracted focused classification and refinement technique (Figure S2B) in RELION 2.1 (Bai et al., 2015; Chowdhury et al., 2017). The whole complex was divided into three regions with some overlap between contiguous regions. These were the head-Cas8f helix bundle-Cas7f.1-Cas7f.2 subunits (region-1), the backbone comprising of all six Cas7f subunits and target DNA bound crRNA (region-2), and the tail-Cas7f.6 subunits (region-3). Each of the signal-subtracted particle stacks were subjected to independent 3D refinement and clustering (classification without alignment) runs, resulting in better quality map for each of the three regions. The final focused map for the head-Cas8f helix bundle-Cas7f.1 subunits, tail-Cas7f.6 subunits, and the backbone region were resolved to 3.3 \AA , 3.2 \AA and 3.1 \AA (at 0.143 FSC value) (Figure S3F), respectively. In order to better facilitate model building of the full Csy-DNA complex, the three focused maps were aligned relative to each other, with the overlapping regions and the unsharpened non-focused reconstructed map of the full complex serving as guides and alignment references. A composite map was generated from the three focused maps by retaining the maximum valued voxel at each point, accomplished by using the “vop maximum” function in UCSF Chimera (Goddard et al., 2007) (Figure S2B). Local resolution estimations (Figure S1E) were calculated using the “bloccres” function in the Bsoft suite (Heymann and Belnap, 2007).

Atomic model building

The atomic models for Cas5f, Cas8f, Cas6f and Cas7f from the Csy-Acr complex (PDB ID: 5UZ9) were used as initial template models for model building. These were individually rigid-body fitted into the reconstructed maps using the “fit map” function in UCSF Chimera (Goddard et al., 2007), and residue registers and backbone geometries were adjusted in Coot (Emsley and Cowtan, 2004). Models for the crRNA and DNA strands were also manually built into the map using Coot. Regions of the map, particularly flexible loop regions could not be modeled due to lack of EM density. Density for the R-loop of the target DNA was not resolved well enough to observe the bases, but position and direction of the sugar-phosphate backbone was sufficient to model (see Figure S3). The atomic model underwent real-space refinement with rigid body fitting and simulated annealing in PHENIX (Afonine et al., 2012). The refined model was used as a seed for generating 200 models in Rosetta and the top scoring model was used for further refinement. Multiple rounds of refinement of the model was performed in PHENIX and Coot to fix the geometric and steric outliers, which were identified by MolProbity during validation. Once the major issues with the model were fixed, the final refinement iterations were carried out with secondary structure and Non-Crystallographic Symmetry (NCS) restraints. The final model was subjected to a multi-model pipeline (Herzik et al., 2019), which produced five models that provided a per-residue assessment of the quality of the EM density. Residues with high $C\alpha$ RMSDs ($> 3\text{\AA}$) were truncated to the $C\beta$ or removed from the atomic model prior to deposition. UCSF Chimera (Goddard et al., 2007) and ChimeraX (Goddard et al., 2018) were used for visualization and for generating all the figures for the maps and models (Figures S3A–S3E and S3G).

All the maps and atomic model (Table S2) were deposited into EMDDataBank and Protein Data Bank with accession codes EMD-9191 and PDB ID 6NE0, respectively.

EMSAs

dsDNA binding assay

Binding assays were performed by incubating 0, 0.001, 0.01, 0.05, 0.1, 0.5, 1, 10, 100, 1000, 10,000 nM Csy complex with < 0.5 nM of 5' ³²P-labeled DNA oligonucleotides for 15 minutes at 37 °C in reaction buffer (20 mM HEPES pH 7.5, 100 mM KCl, 5% glycerol, 1 mM TCEP). Reaction products were run on 6% polyacrylamide gels, which were dried and imaged with a phosphor storage screen (Kodak), then scanned with a Typhoon phosphorimager (GE Healthcare). Bands were quantified using ImageQuant software, and the percent DNA bound was plotted as a function of Csy complex concentration, then fit with a standard binding isotherm: Fraction DNA bound = [Csy complex]/(K_D + [Csy complex])

Cas1-2/3 recruitment assay

5' [³²P]-labeled 80-base pair dsDNA (Table S1) was pre-incubated with 1 μM Csy complex at 37°C in reaction buffer (20 mM HEPES pH 7.5, 100 mM KCl, 5% glycerol, 1 mM TCEP, 5 mM MgCl₂, 75 μM NiSO₄, 5 mM CaCl₂, 1 mM ATP) for 15 minutes. Reactions were then moved to ice, and KCl concentration was increased to 300 mM to reduce non-specific interactions between DNA and Cas1-2/3. 1.85 nM, 5.5 nM, 16.6 nM, or 50 nM Cas1-2/3 was added to reactions, which were incubated for a further 5 minutes at 37°C. Reactions were separated by electrophoresis over native 4.5% polyacrylamide gels. Dried gels were imaged with a phosphor storage screen (Kodak), scanned with a Typhoon phosphorimager (GE Healthcare), and band intensities were quantified using ImageQuant software (GE Healthcare).

QUANTIFICATION AND STATISTICAL ANALYSIS

Cryo-EM data collection, refinement, and validation statistics are reported in Table S2. All biochemical experiments were conducted with at least 3 independent replicates (n = 3), and error bars represent the standard error of the mean.

DATA AND SOFTWARE AVAILABILITY

The electron microscopy density map has been deposited in the EM Data Bank (EMDB: 9191) and an atomic model has been deposited in the Protein Data Bank (PDB: 6NE0). Plasmids used for overexpression and purification of the Csy complex and Cas1-2/3 complex have been deposited at Addgene (see Key Resources Table).